 doi:10.20944/preprints201608.0080.v1

Article

A Mathematical Spline-Based Model of Cardiac Left Ventricle Anatomy and Morphology §

Sergei Pravdin [1,2]

[1] Krasovskii Institute of Mathematics and Mechanics, Ural Branch of Russian Academy of Science, 620990 Ekaterinburg, Russia; sfpravdin@imm.uran.ru

[2] Ural Federal University, 19 Mira street, 620002 Ekaterinburg, Russia

§ This paper is an extended version of our paper published in S. Pravdin. A mathematical model of cardiac left ventricle anatomy and morphology. Abstracts of «Experimental and computational biomedicine»: Russian Conference with International Participation in memory of Professor Vladimir S. Markhasin. 2016. P. 25.

Abstract: Computer simulation of normal and diseased human heart activity requires a 3D anatomical model of the myocardium, including myofibres. For clinical applications, such a model has to be constructed based on routine methods of cardiac visualisation such as sonography. Symmetrical models are shown to be too rigid, so an analytical non-symmetrical model with enough flexibility is necessary. Based on previously made anatomical models of the left ventricle, we propose a new, much more flexible spline-based analytical model. The model is fully described and verified based on DT-MRI data. We show a way to construct it on the basis of sonography data. To use this model in further physiological simulations, we propose a numerical method to utilise finite differences in solving the reaction-diffusion problem together with an example of scroll wave dynamics simulation.

Keywords: left ventricle; myofibre; myocardium structure; rule-based model; mathematical anatomy.

MSC: 92-08

1. Introduction

This model is a further development of another non-symmetrical model of the left ventricle (LV) of the heart [1], which considers meridional sections of the LV and approximates its subepicardial and subendocardial borders by simple curves in sectional coordinates. The curves consist of one or two parts, each defined as a power function of a «latitude» ψ. If both parts are used, an LV-dividing region «equator» is identified where the LV is mostly distanced from the vertical axis.

A new model must be constructed because, in many situations, a well-fitting LV model cannot be made. We faced this when we tried to make «power-function» models using sonography and tomography data of human hearts.

The new model uses splines instead of power functions and, as we will show in this paper, is flexible enough to fit real medical visualisation data. At the same time, the new model uses analytical calculations, so some of the derivatives necessary for solving reaction-diffusion systems can be found exactly. In the proposed model, both anatomy and fibre direction field are defined analytically. We calculate fibre slope angles in a local coordinate system and compare them with *in vitro* experimental data on human hearts.

2. Construction of the LV model

In order to define the LV form, we use a special coordinate system (γ, ψ, ϕ), where the variable $\gamma \in [0,1]$ corresponds with position of a point in the LV wall layer: $\gamma = 0$ is the endocardium, $\gamma = 1$ is the epicardium, $\psi \in [0, \pi/2]$ is an analogue of latitude, $\psi = 0$ is the upper plane part of the LV model (fibrous ring and valve zone), $\psi = \pi/2$ is the LV apex, and $\phi \in [0, 2\pi)$ is an analogue of longitude.

Preprints (www.preprints.org) | NOT PEER-REVIEWED | Posted: 8 August 2016 doi:10.20944/preprints201608.0080.v1

Initial data for the model construction are

1. meridians ϕ_i, $i = 0, 1, \ldots n-1$, where measurements are taken;
2. coordinates $\rho^{epi}_{i,j}$, $z^{epi}_{i,j}$, $i = 0, 1, \ldots n-1$, $j = 0, 1, \ldots n^{epi}_i - 1$, of *marked* points on the epicardium;
3. coordinates $\rho^{endo}_{i,j}$, $z^{endo}_{i,j}$, $i = 0, 1, \ldots n-1$, $j = 0, 1, \ldots n^{endo}_i - 1$, of *marked* points on the endocardium.

Now we describe our algorithm to construct the LV model. First, for each meridian of the epicardium, we connect the marked points by an interpolation curve (Fig. 1). We obtain a set of n curves in this step. Second, for each latitude ψ, we connect the n points on the curves by a closed interpolation curve. Algebraically, this means that we use a periodic spline. We obtain an epicardial surface in this step. Next, we do the same for the endocardium and, finally, we fill the space between the epi- and endocardium by a linear function of γ.

This schema can be formalised using the following equations. To transform the special coordinates into cylindrical ones (ρ, ϕ, z), we use a simple formula for z-coordinate transformation:

$$z(\gamma, \psi) = Z - (Z - h\gamma)\sin\psi, \tag{1}$$

where Z is the LV height, and h is the LV wall thickness at the apex. Using this formula, we calculate ψ-coordinates of the marked points:

$$\psi(\gamma, z) = \arcsin\left(\frac{Z - z}{Z - h\gamma}\right). \tag{2}$$

As mentioned above, $\gamma = 0$ on the epicardium, and $\gamma = 1$ on the endocardium.

In each section ϕ_i on the epicardium (endocardium), we make an epicardial (endocardial) curve

$$\rho^{epi}(\psi, \phi_i) = \mathrm{spline}(\psi; \psi^{epi}_{i,j} \mapsto \rho^{epi}_{i,j}), \qquad \rho^{endo}(\psi, \phi_i) = \mathrm{spline}(\psi; \psi^{endo}_{i,j} \mapsto \rho^{endo}_{i,j}). \tag{3}$$

Here, spline is a cubic spline with zero second derivative at the endpoints. The notation $\mathrm{spline}(x; x_i \mapsto y_i)$ means a spline constructed by two given arrays of data, x_i as an argument and y_i as a response variable. Then, we interpolate to obtain a surface between the curves:

$$\rho^{epi}(\psi, \phi) = \mathrm{spline}(\phi; \phi_i \mapsto \rho^{epi}(\psi, \phi_i)), \qquad \rho^{endo}(\psi, \phi) = \mathrm{spline}(\phi; \phi_i \mapsto \rho^{endo}(\psi, \phi_i)). \tag{4}$$

Here, we use a periodic cubic spline. And finally, we fill the entire LV wall:

$$\rho(\gamma, \psi, \phi) = \rho^{epi}(\psi, \phi)(1 - \gamma) + \rho^{endo}(\psi, \phi)\gamma. \tag{5}$$

Usually, if n meridional sections are considered, the angles between them are uniform, so $\phi_i = i\pi/n$, $i = 0, 1, \ldots n-1$.

2.1. Spiral surfaces

Hierarchically, the LV model is subdivided into muscle layers. In its turn, each layer is filled by myofibres. All the layers have a spiral-like shape so we call them «spiral surfaces» (SS). These surfaces have the same equation in special coordinates:

$$\phi(\gamma, \phi_{\min}, \phi_{\max}) = \phi_{\min} + \gamma\phi_{\max}, \tag{6}$$

where $\phi_{\max}$ is the SS twist angle (which is the same for all SS), and different values of $\phi_{\min} \in [0, 2\pi)$ determine different surfaces. The equation of the SS in the cylindrical coordinates is shown below (see (5), (1)).

$$\rho_{sp}(\psi, \phi, \phi_{\min}) = \rho\left(\frac{\phi - \phi_{\min}}{\phi_{\max}}, \psi, \phi\right); \tag{7}$$

Preprints (www.preprints.org) | NOT PEER-REVIEWED | Posted: 8 August 2016 doi:10.20944/preprints201608.0080.v1

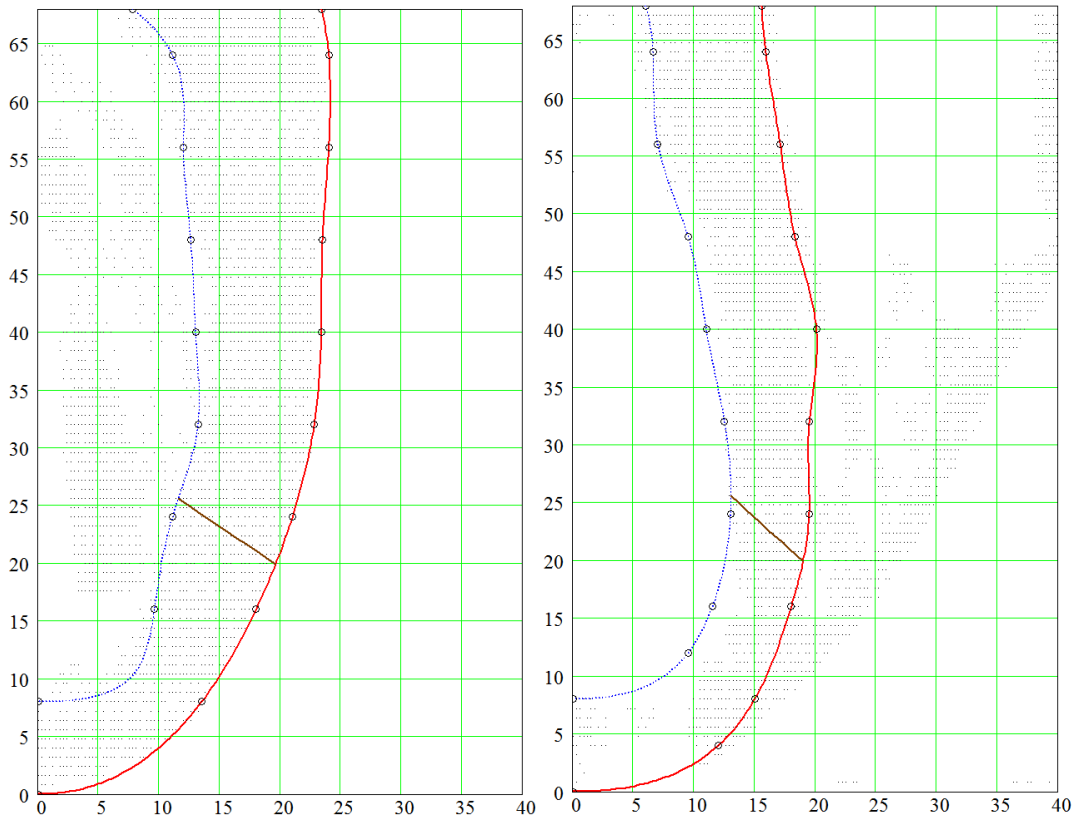

Figure 1. Vertical (meridional) sections of the LV free wall (on the left) and the IVS (on the right) of a human heart. The points represent DT-MRI data; the solid red line represents the model epicardium; the dashed blue line represents the model endocardium. The circles show the interpolation (marked) points given by a user. The horizontal axis is ρ; the vertical axis is z. On the right panel, we see a papillar muscle in the RV cavity (vertical one, $\rho = 25 \ldots 45$ mm) and an RV free wall (inclined).

$$z_{sp}(\psi, \phi, \phi_{\min}) = z\left(\frac{\phi - \phi_{\min}}{\phi_{\max}}, \psi\right). \tag{8}$$

2.2. Filling a spiral surface with fibres

We have utilised J. Pettigrew's proposal [2] as we did in our previous models [1,3]. This proposal has been chosen because it can be formalised easily, and it describes both myofibres and sheets. Myocardial fibres are obtained as images of chords $Y = \text{const}$, $Y \in [0,1)$ of sector $\mathrm{P} \le 1$, $\Phi \in [\pi\gamma_0, \pi\gamma_1]$ (the chords are parallel to the diameter $Y = 0$) on the SS (Fig. 2). Here, γ_0 and γ_1 $(0 \le \gamma_0 < \gamma_1 \le 1)$ are necessary parameters to fit the sub-epicardial and sub-endocardial fibre angles. The parameter of any chord is the polar angle $\Phi \in [\Phi_0, \Phi_1]$, where $\Phi_0 = \max(\arcsin Y, \pi\gamma_0)$ and $\Phi_1 = \min(\pi - \arcsin Y, \pi\gamma_1)$. The mapping of a chord point (P, Φ) to an SS point is defined by the formulae below (Fig. 3):

$$\gamma(\Phi) = \frac{\Phi - \pi\gamma_0}{\pi(\gamma_1 - \gamma_0)},$$
$$\psi(\mathrm{P}) = (1 - \mathrm{P}) \cdot \frac{\pi}{2}.$$

For instance, if $\gamma_0 = 0$ and $\gamma_1 = 1$, the semicircle diameter is transformed into a fibre that begins on the basal epicardium, descends to the apex $(\Phi = \pi/2)$, then ascends and ends on the basal endocardium. Images of shorter chords are located closer to the LV base and have shorter lengths.

Preprints (www.preprints.org) | NOT PEER-REVIEWED | Posted: 8 August 2016 doi:10.20944/preprints201608.0080.v1

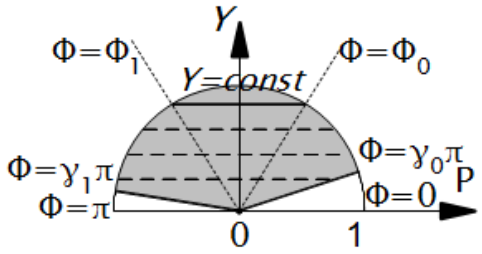

Figure 2. Horizontal chords on the sector $P \le 1$, $\Phi \in [\pi\gamma_0, \pi\gamma_1]$. Here, Φ_0 and Φ_1 are polar angles of the right and left chord ends, respectively. Parameter $\gamma_0 = 0.1$ and $\gamma_1 = 0.95$.

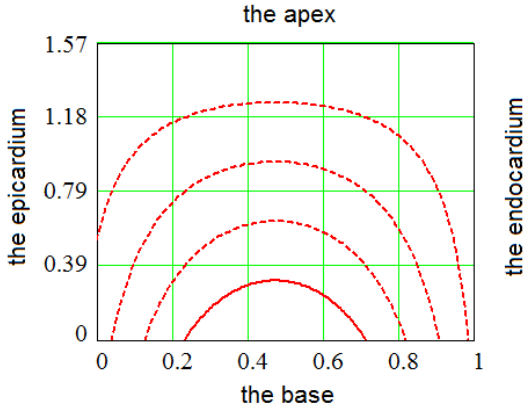

Figure 3. Images of the sector chords in (γ, ψ) coordinates. The horizontal axis is γ, and the vertical axis is ψ. Parameter $\gamma_0 = 0.1$ and $\gamma_1 = 0.95$.

2.3. Calculation of the fibre direction in points of the LV model

In practical applications of cardiac anatomical models, it is necessary to compute a vector of fibre direction in a point whose position is given in a Cartesian coordinate system. Let the point coordinates be (x, y, z). One can easily convert them into cylindrical coordinates (ρ, ϕ, z). The vector of fibre direction can be found using the following algorithm:

1. Use formula (5) to find the special coordinates γ and ψ of the point numerically. This problem can be reduced to solving one algebraic equation with one unknown quantity γ on the segment $[0, 1]$. We utilise the expression for $\psi(\gamma, z)$ from formula (1) and substitute it into (5):

$$\rho = \rho^{epi}(\psi(\gamma, z), \phi)(1 - \gamma) + \rho^{endo}(\psi(\gamma, z), \phi)\gamma.$$

   We solve this equation with respect to γ. Let the root be γ. Hence, the point's special coordinate $\psi = \arcsin\left(\frac{Z-z}{Z-h\gamma}\right)$.
2. Differentiate (numerically or analytically) the function $\rho(\gamma, \psi, \phi)$ with respect to all arguments and obtain three partial derivatives ρ_γ, ρ_ψ, and ρ_ϕ. We can find one derivative analytically:

$$\rho_\gamma = \rho^{endo}(\psi, \phi) - \rho^{epi}(\psi, \phi).$$

3. The LV model point is an image of a point on the sector $P \le 1$, $\Phi \in [\pi\gamma_0, \pi\gamma_1]$. This point, the preimage, has polar coordinates $P = 1 - \frac{2\psi}{\pi}$, $\Phi = \pi\gamma(\gamma_1 - \gamma_0) + \pi\gamma_0$ and Cartesian coordinates $X = P\cos\Phi$, $Y = P\sin\Phi$.
4. The LV point $\vec{r}$, parameterised by Φ, has Cartesian coordinates

$$x(\Phi) = \rho(\gamma(\Phi), \psi(P(\Phi)), \phi(\gamma(\Phi), \phi_{\min}, \phi_{\max}))\cos\phi(\gamma(\Phi), \phi_{\min}, \phi_{\max}),$$

Preprints (www.preprints.org) | NOT PEER-REVIEWED | Posted: 8 August 2016 doi:10.20944/preprints201608.0080.v1

$$y(\Phi) = \rho(\gamma(\Phi), \psi(\mathrm{P}(\Phi)), \phi(\gamma(\Phi), \phi_{\min}, \phi_{\max})) \sin\phi(\gamma(\Phi), \phi_{\min}, \phi_{\max}),$$
$$z(\Phi) = \rho(\gamma(\Phi), \psi(\mathrm{P}(\Phi))),$$

where $\phi_{\min} = \phi - \gamma\phi_{\max}$, $\mathrm{P}(\Phi) = Y/\sin\Phi$.

5. The non-normalized vector $\vec{w} = (wx, wy, wz) = \frac{d\vec{r}}{d\Phi}$ of the fibre direction has components

$$wx = \frac{\sin\Phi}{(\pi - 2\psi)(\gamma_1 - \gamma_0)} \cdot \left(y\phi_{\max} - (\rho_\gamma + \rho_\phi\phi_{\max}) \cdot \cos\phi\right) - \cos\phi \cdot \rho_\psi \cdot \frac{\pi}{2} \cdot \cos\Phi,$$
$$wy = \frac{\sin\Phi}{(2\psi - \pi)(\gamma_1 - \gamma_0)} \cdot \left(x\phi_{\max} + (\rho_\gamma + \rho_\phi\phi_{\max}) \cdot \sin\phi\right) - \sin\phi \cdot \rho_\psi \cdot \frac{\pi}{2} \cdot \cos\Phi,$$
$$wz = \frac{h\sin\Phi\sin\psi}{(2\psi - \pi)(\gamma_1 - \gamma_0)} + (Z - h\gamma)\cos\psi \cdot \frac{\pi}{2} \cdot \cos\Phi.$$

2.4. Fitting the LV form

In the paper [1], a fitting of the more rigid model to a real canine heart dataset was done with satisfactory results. Yet, fitting the dataset of a human heart into that model was less successful, partially due to the limitations of the model's parameters. In this study, the same dataset of the human heart was used for the flexible model. The dataset is accessible online at

`http://gforge.icm.jhu.edu/gf/project/dtmri_data_sets/docman/`

The fitting procedure began with finding the LV axis Oz. Then, we sectioned the LV by $N = 12$ meridional half-planes $\phi_i = 2\pi i/N$, $i = 0, 1 \ldots N-1$, passing this axis, and we manually marked points on the epi- and endocardium in each section. The mean numbers of points were 10 for the sub-endocardium and 11 for the sub-epicardium. In total, taking into account the coincidence of two apical points in all the sections, there were 227 points. After setting the points, we used periodic cubic ϕ-splines and cubic ψ-splines.

3. Methods for model and experimental data comparison

In the work [1], the theoretical model and experimental data were compared along normals to epicardial meridional sections as described in [4]. However, this method is not useful: normals do not have to intersect the endocardium, and they may intersect each other, so the task of finding a normal passing through a point may result in multiple solutions. In the present article, we use the special coordinates to construct straight *pinning* lines that do not intersect each other and always intersect the endocardium. These lines have a simple equation: $\psi = \text{const}$, $\phi = \text{const}$.

We will now describe the comparison procedure. To compare angles along such a pinning line, one needs to specify a point A on the epicardium. Let its special coordinates be $\gamma = 0$, $\psi = \psi^*$ and $\phi = \phi^*$. Let us consider a corresponding meridional section $\phi = \phi^*$ of the model, semiplane Π. The line lies in Π and intersects the endocardium at a point B, having coordinates $\gamma = 1$, $\psi = \psi^*$ and $\phi = \phi^*$. On the segment AB, we set k unidistant points, including its ends, so that $A = A_1, A_2, \ldots, A_k = B$. The position of a point A_i on the segment AB is defined by the variable

$$t_i = \frac{A_iB}{AB}$$

(for the endocardium $t = 0$, for the epicardium $t = 1$). We have to draw an SS through every point $A_i(\gamma_i = (i-1)/(k-1), \psi^*, \phi^*)$. The problem of finding such an SS is reduced to solving the SS equation (6) with respect to $\phi_{\min}$:

$$\phi_{\min} = \phi^* - \gamma_i\phi_{\max}.$$

Strictly speaking, there can be no points from the tomogram exactly on semiplane Π; therefore, we selected points lying no further than $\Delta = 1$ mm from the straight line AB and inside the dihedral angle $|\phi - \phi^*| \le \Delta_\phi = 0.1$ rad$= 5.7^\circ$.

Preprints (www.preprints.org) | NOT PEER-REVIEWED | Posted: 8 August 2016 doi:10.20944/preprints201608.0080.v1

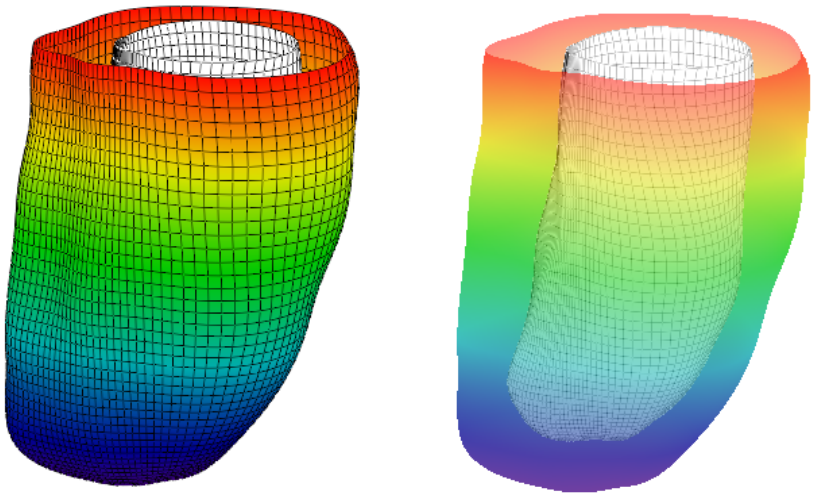

Figure 4. Epicardial and endocardial surfaces of the model that was constructed based on DT-MRI data. On the left, the epicardium is opaque. On the right, the epicardium is semi-transparent. Colour shows z-coordinates.

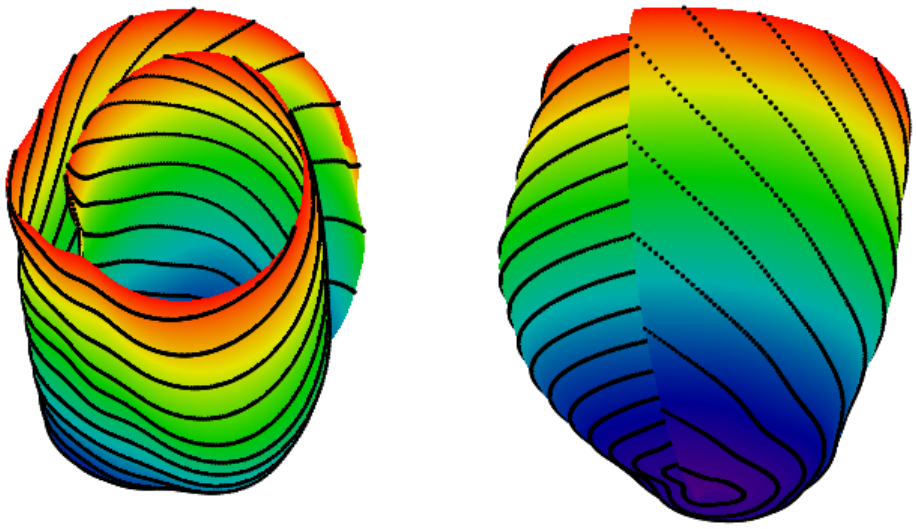

Figure 5. A spiral surface (SS) with fibres on it. Two views are shown. The left of the figure depicts a view from the top and side of the SS, while the right of the image provides a side view with the mid-myocardial part on the left and the epicardial layer on the right. Colour shows z-coordinates.

Preprints (www.preprints.org) | NOT PEER-REVIEWED | Posted: 8 August 2016 doi:10.20944/preprints201608.0080.v1

Streeter proposed specifying a fibre direction using a local coordinate system (u, v, w) and two angles, 'true fibre angle' α and 'helix angle' α_1 [4, p. 78] (see Fig. 6); these angles are sufficient for specifying a fibre direction in a point. The axis u is a normal to the epicardium pointed away from the LV; w is a meridian, i.e. an epicardial tangent lying in a meridional semiplane and pointed upwards; v is a parallel, i.e. vector $w \times u$. Angle $\alpha \in [0, \pi/2]$ is between a fibre and the parallel, and angle $\alpha_1 \in [-\pi/2, \pi/2]$ is between the fibre projection on the plane uv and the parallel.

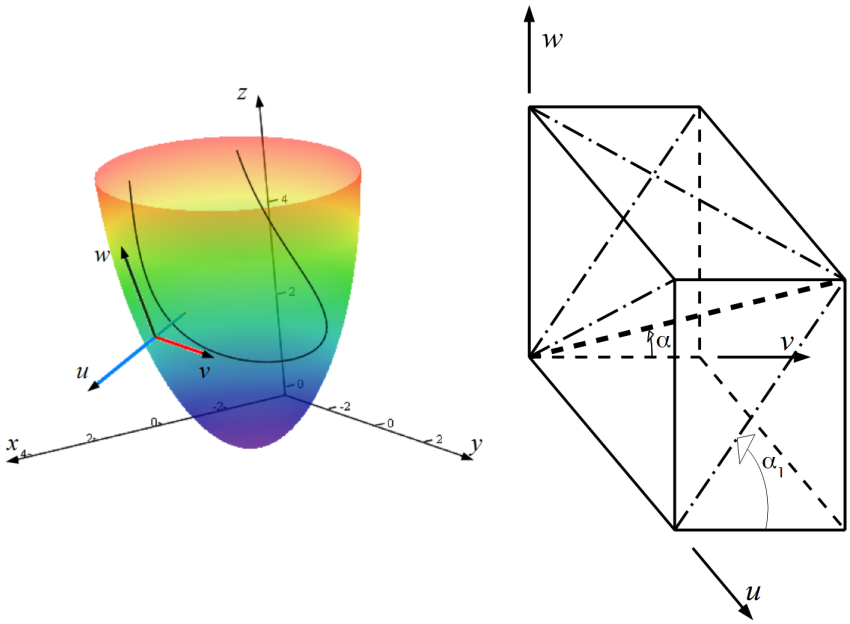

Figure 6. The definition of the local coordinate system is shown on the left of the image. *Oxyz* is the global Cartesian coordinate system. The blue axis is normal, u, to the epicardium. The red axis is parallel tangent, v. The dark green axis is meridian tangent, w. The colourful surface is the epicardium; the colour depends on altitude z. The curve inside is a model fibre and it does not lie on the epicardium. The normal axis intersects the curve at a point. On the right, the definitions of the true fibre angle α and the helix angle α_1 are shown. The thick, dashed line is a tangent to a myofibre segment constructed at the origin of the coordinates. The dashed-and-dotted lines are projections of the myofibre tangent.

We changed 'normal' in these definitions to 'pinning line' and compared the two angular characteristics of fibre directions with the experimental data in two meridians (one meridian lies in the LV free wall, another lies in the IVS) in upper, middle and lower parts of the LV wall.

4. Results of comparing the model with human heart data

The following parameter values, which are common for all meridians, were used: LV height $Z = 68$ mm, LV wall thickness at the apex $h = 8$ mm, SS twisting angle $\phi_{\max} = 3\pi$, endocardial fibre parameter $\gamma_0 = 0.13$ and epicardial fibre parameter $\gamma_1 = 0.9$.

4.1. Comparison along straight pinning lines

Graphs of the dependency of angles α, α_1 on a point position on pinning lines are shown in Figs. 7–12. We will now analyse the results obtained.

At the upper and middle LV areas (e.g., Figs. 7 and 8, *A*), one can see that the vertical axis does not go through the centre of the horizontal LV sections, but it is situated closer to the IVS. The axis is positioned there because it must go through the apical LV area, and the LV apex projection to its basal

Preprints (www.preprints.org) | NOT PEER-REVIEWED | Posted: 8 August 2016 doi:10.20944/preprints201608.0080.v1

plane is not situated at the centre of the base. If one moves the axis to the base centre, then the apex is far from the axis in one of the meridional sections; therefore, we cannot fit the LV wall shape using the central position of the axis.

Let us consider the fibre slope angles in one of the LV free-wall meridians. In the upper LV part (see Fig. 7), the true fibre angle α (panel *C*) in the model accurately reproduces the DT-MRI data. Angle α descends from 75° on the endocardium to approximately 15° at the middle of the wall, then it reaches 65° on the epicardium. The helix angle (panel *D*) in the model is also quite close to the experimental data. The middle part of the free wall, which is determined by height (see Fig. 8), shows an essentially large dispersion of the both angles' values in the subendocardial zone ($x < 0.2$). These angles' values are similar to those in the basal zone, so the model can reproduce them well. The angles at the lower part of the LV free wall (see Fig. 9) are predicted by the model with slightly lesser accuracy.

In the upper part of the IVS (see Fig. 10), the model behaves in a different way than the experimental data. In the middle part of the IVS (see Fig. 11), the model reproduces the angles reasonably accurately. Fig. 12 shows that the model simulates the angles in the interior part of the myocardium better than in the exterior part.

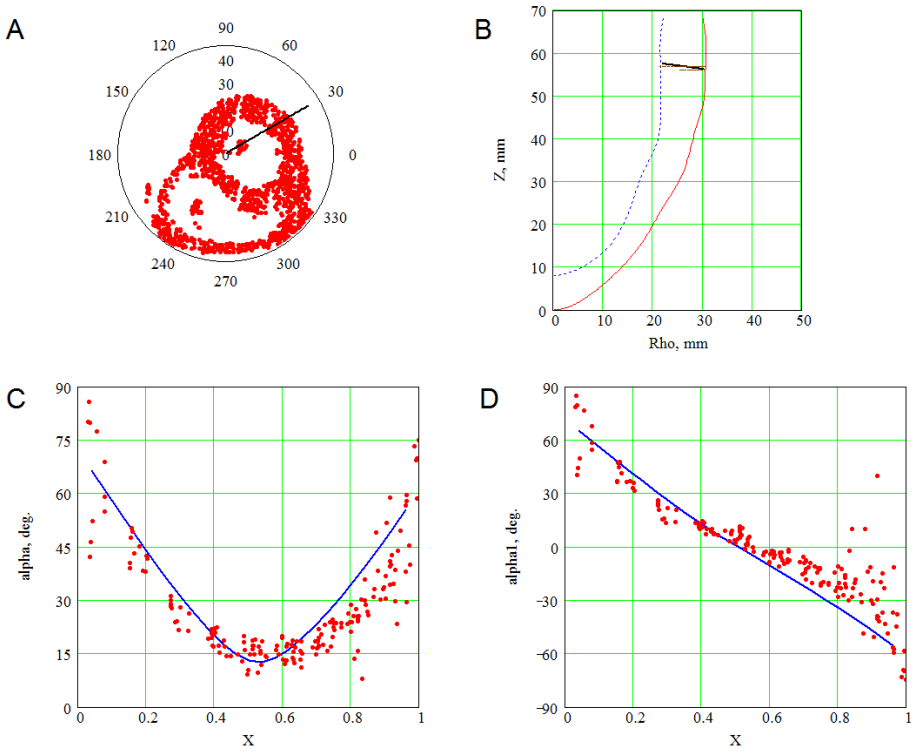

Figure 7. Fibre angles in the model and in the experimental data. The basal area ($\psi = 10°$) of the LV free wall is shown. *A* is a horizontal LV section. The points are myocardial points from a DT-MRI scan. *B* is a meridional LV section. The solid (dashed) curve is the model epicardium (endocardium), and the points are myocardial points from a DT-MRI scan. *C* and *D* show the angles α and α_1, respectively. The *X*-axis displays the position of points in the wall depth; 0 corresponds to the endocardium, and 1 corresponds to the epicardium. The points show the experimental data, while the curves show the model data.

If one considers the fibres in the radial direction, our model (like the model from [3]) imitates the distinctive arrangement of fibres in the ventricular wall (see [3], Fig. 14). This arrangement was called the "Japanese fan" by Streeter (see [4], Fig. 42, *C*).

Preprints (www.preprints.org) | NOT PEER-REVIEWED | Posted: 8 August 2016 doi:10.20944/preprints201608.0080.v1

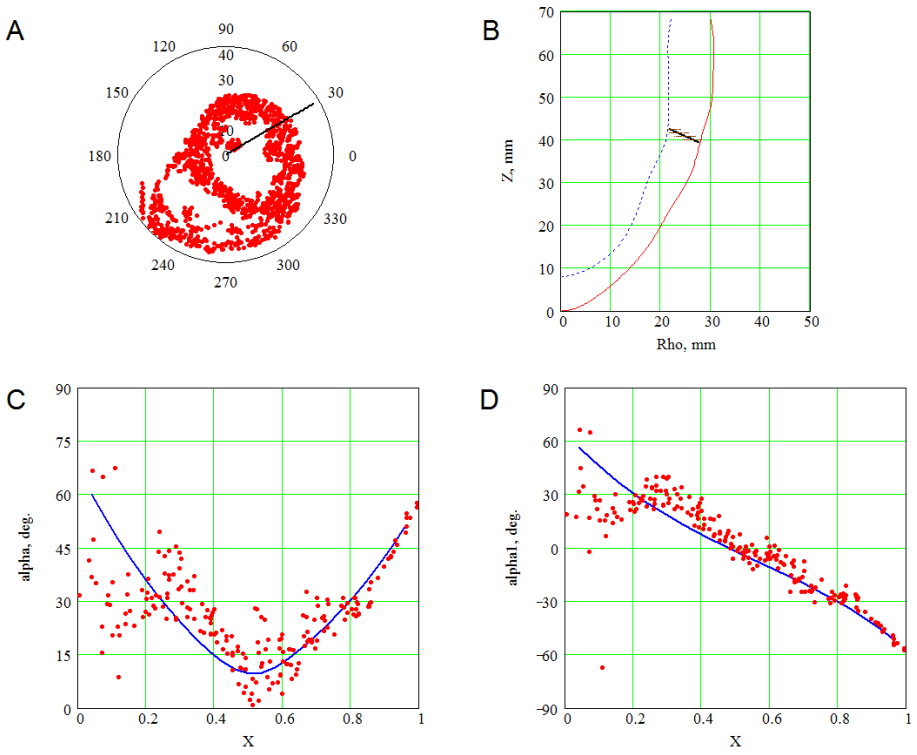

Figure 8. Fibre angles in the model and experimental data. The LV free wall in the middle area ($\psi = 25°$) is shown. The conventional signs are the same as in Fig. 7.

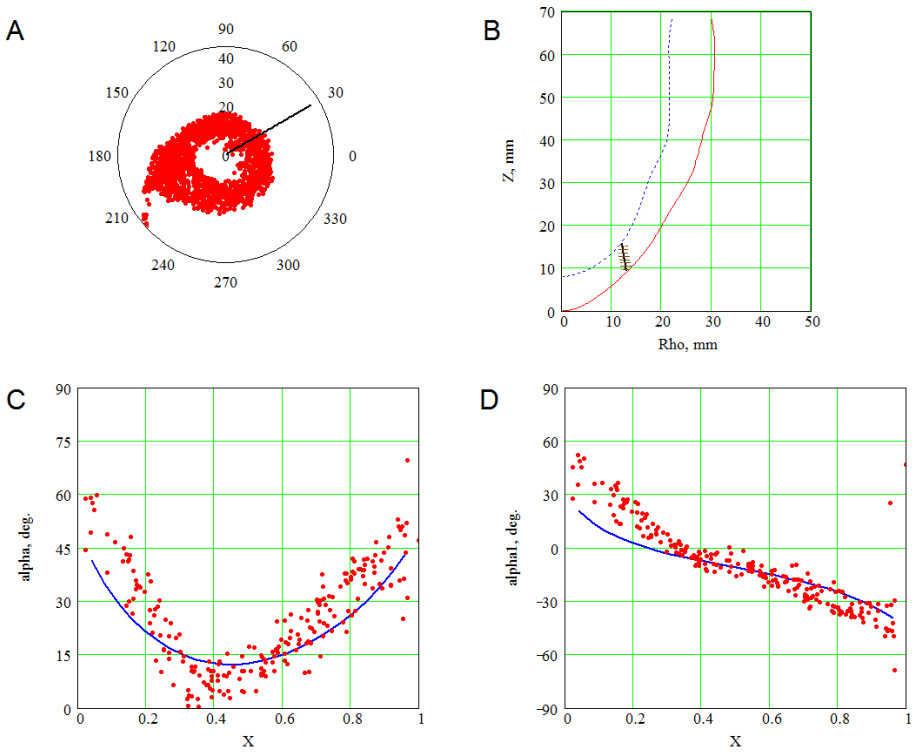

Figure 9. Fibre angles in the model and experimental data. The LV free wall in the apical area ($\psi = 60°$) is shown. The conventional signs are the same as in Fig. 7.

Preprints (www.preprints.org) | NOT PEER-REVIEWED | Posted: 8 August 2016 doi:10.20944/preprints201608.0080.v1

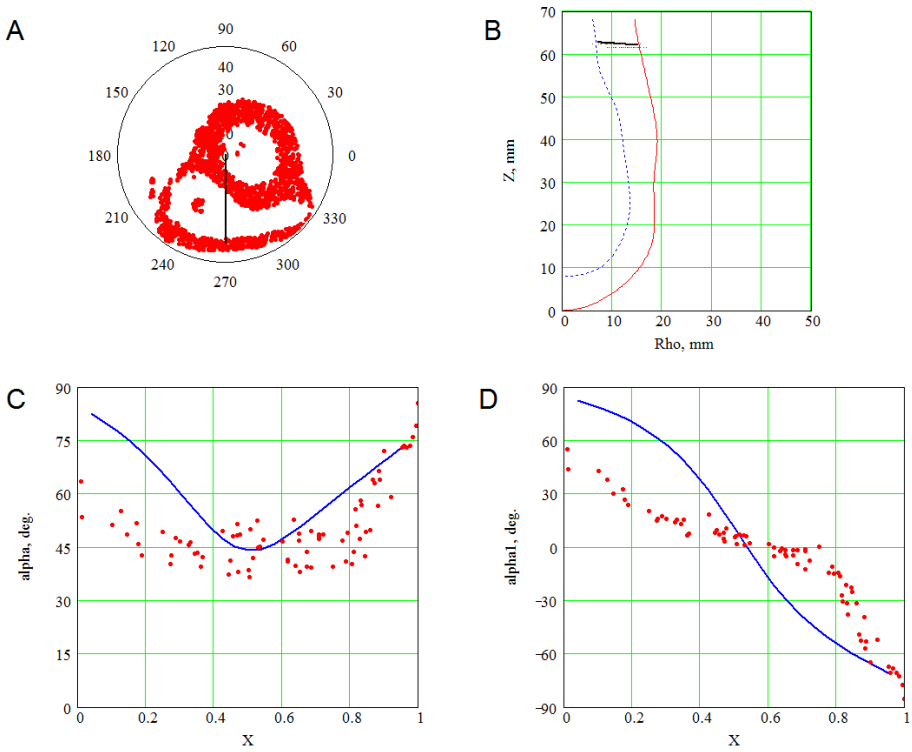

Figure 10. Fibre angles in the model and experimental data. The IVS in the basal area ($\psi = 5°$) is shown. The conventional signs are the same as in Fig. 7.

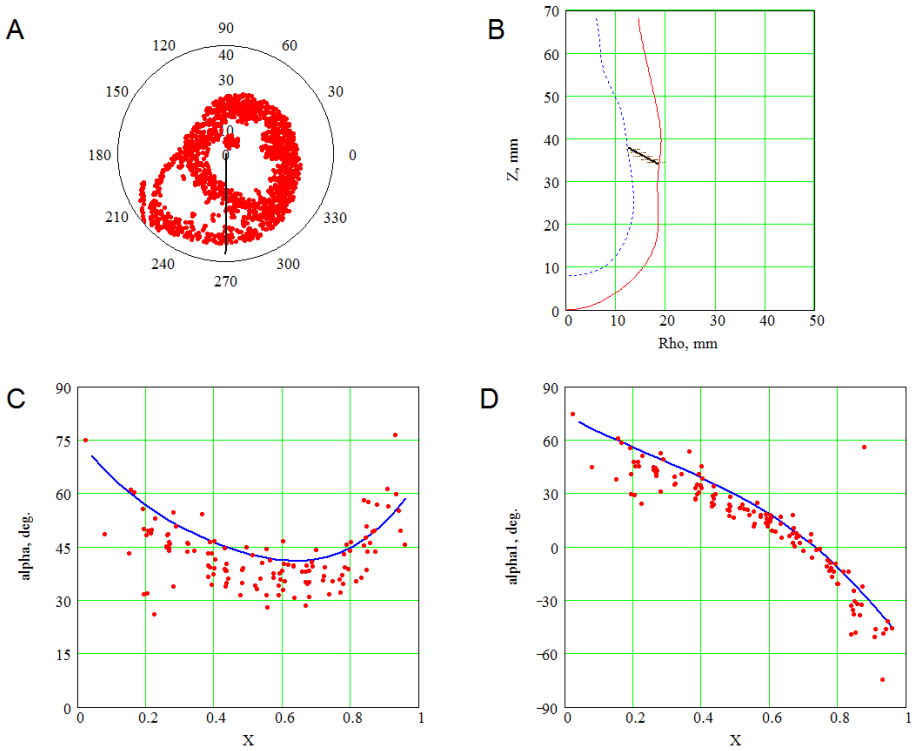

Figure 11. Fibre angles in the model and experimental data. The IVS in the middle area ($\psi = 30°$) is shown. The conventional signs are the same as in Fig. 7.

Preprints (www.preprints.org) | NOT PEER-REVIEWED | Posted: 8 August 2016 doi:10.20944/preprints201608.0080.v1

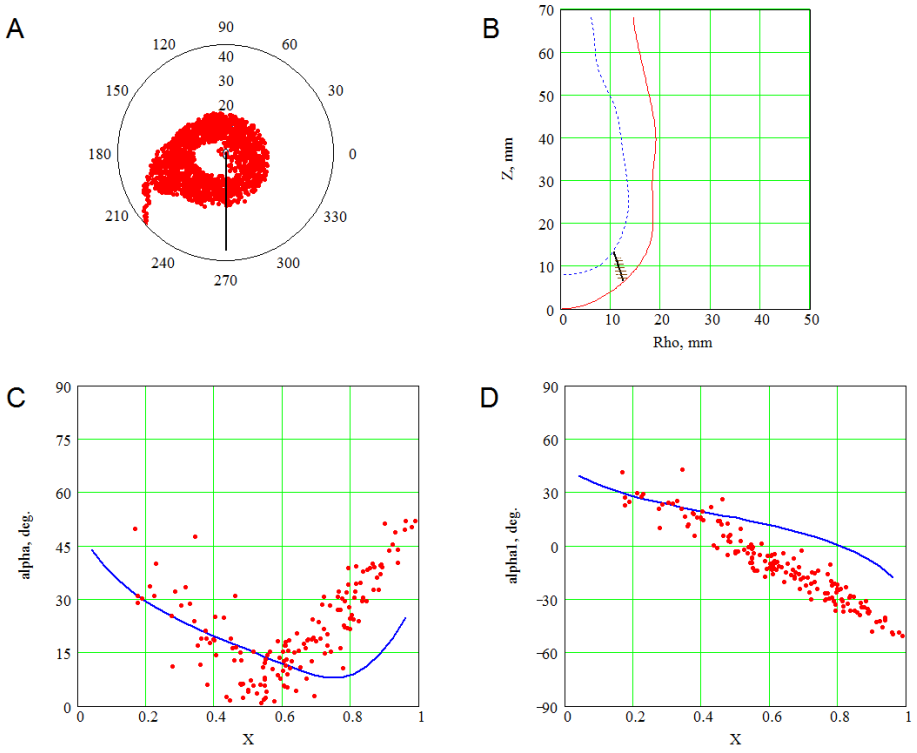

Figure 12. Fibre angles in the model and experimental data. The IVS in the apical area ($\psi = 65°$) is shown. The conventional signs are the same as in Fig. 7.

4.2. 3D verification

We compared the fibre directions of the tomography dataset and the model in all DT-MRI points located inside the model LV wall, and we made a histogram of the results (Fig. 13). The mean angle between the two directions is 21° and the median is 15°.

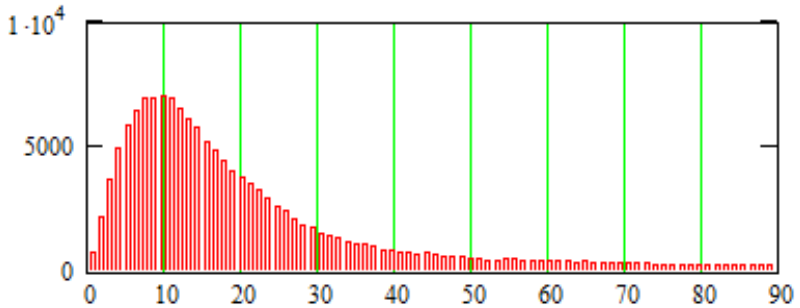

Figure 13. Histogram of angles between fibres in experiment and model data. X-axis is the angle; Y-axis is the number of points in the segments; the segment $[0, 90°]$ was divided into 100 segments of equal length.

We can conclude that our model reproduces the fibre directions adequately.

Preprints (www.preprints.org) | NOT PEER-REVIEWED | Posted: 8 August 2016 doi:10.20944/preprints201608.0080.v1

5. Constructing a model based on sonography data

The proposed model can be constructed based on sonography data. We made one such measurement using data from two- and four-chamber views of one patient's heart. In Fig. 14, we show a comparison of two models: the old model based on power functions and the present spline-based one. The model was made using 44 marked points, from which 22 were endocardial and 22 were epicardial. Since the right part of the LV wall has a complex curved shape, it cannot be approximated accurately by the first model, but it can be well approximated by the second one. The left part of the LV wall has a simpler shape, so both models can be fitted into it well.

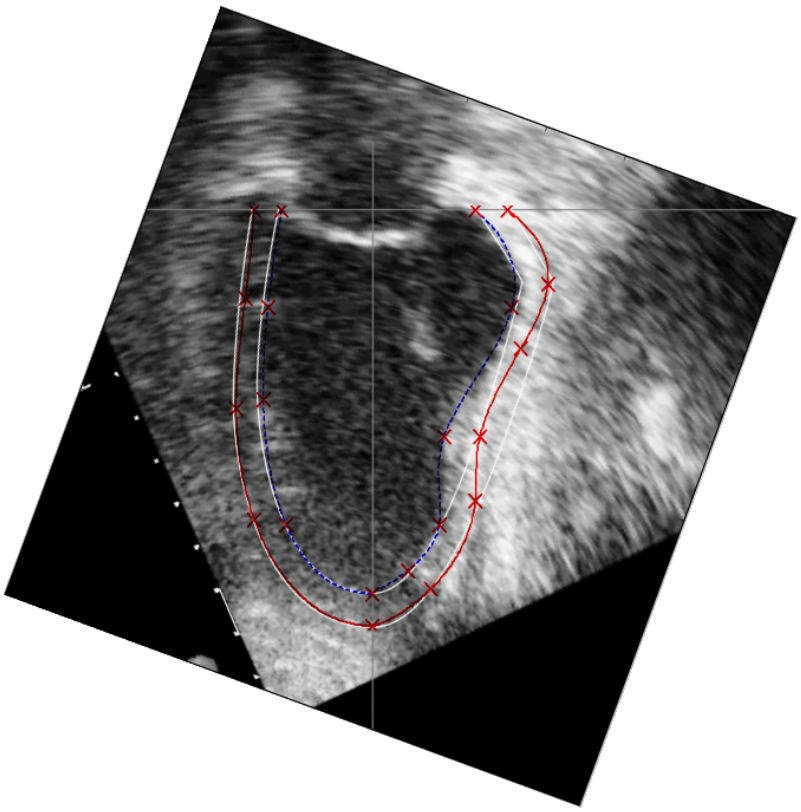

Figure 14. A sonographical two-chamber view of a patient's heart and two measurements: the first for the power-function-based model (white lines) and the second for the spline-based model (blue lines show the endocardium; red lines show the epicardium). The patient suffered from an old myocardial infarction, and a scar is present. The marked points are shown as crosses. This view gives data for two model meridians. The model axis and base are shown as grey lines. The image has been rotated so that the model axis Oz is vertical.

6. Numerical method for solving reaction-diffusion systems on the model

Electrophysiological processes in the myocardium are usually simulated using reaction-diffusion systems of partial differential equations. In the monodomain case, they are

$$\dot{u} = \operatorname{div}(D \operatorname{grad} u) + f(u, \vec{v}), \tag{9}$$

$$\dot{\vec{v}} = \vec{g}(u, \vec{v}). \tag{10}$$

Here, u is the transmembrane potential, $\vec{v}$ is the vector of other phase variables (its components differ in different models), the diffusion matrix D has elements $D_{ij} = D_2\delta^{ij} + (D_1 - D_2)w_i(\vec{r})w_j(\vec{r})$, $i, j = 1, 2, 3$, and $\vec{w}$ is the unit vector of fibre direction.

Preprints (www.preprints.org) | NOT PEER-REVIEWED | Posted: 8 August 2016 doi:10.20944/preprints201608.0080.v1

The boundary condition of zero flux of the potential through the myocardial boundary looks like

$$\vec{n} D \operatorname{grad} u = 0, \tag{11}$$

where $\vec{n}$ is a normal vector to the boundary. In the case of complex cardial shape, implementation of the boundary condition is difficult, and it requires either a special method of Laplacian computation near the boundary in Cartesian coordinates or a special coordinate system where the boundaries are coordinate surfaces.

The LV base, epicardium and endocardium are just coordinate surfaces in the special coordinates linked with this model. Indeed, the base has the equation $\psi = 0$, while the equation $\gamma = \text{const}$ describes the epicardium and endocardium. For the symmetrical LV model, we proposed an algorithm [5] which has been used in a study of scroll wave dynamics [6]. For the previous (power-functions based) non-symmetrical model [1], a modified algorithm has been described elsewhere [7]. That algorithm can be used in the present case as well without any changes. However, since it was not published in English, we depict its dissimilarity with the symmetrical-case method briefly here.

6.1. Formulae for the Laplacian in the special coordinates

Let us denote the special coordinates (γ, ψ, ϕ) uniformly as (ξ_0, ξ_1, ξ_2) and consider matrices

$$\mathbf{J} = (J_{ij}) = \left(\frac{\partial \xi_i}{\partial x_j}\right),$$
$$\mathbf{W} = (W_{ij}) = \left(\frac{\partial v_i}{\partial x_j}\right), \qquad \mathbf{S} = (S_{ij}) = \left(\frac{\partial v_i}{\partial \xi_j}\right),$$
$$\mathbf{T}^k = (T^k_{ij}) = \left(\frac{\partial^2 \xi_k}{\partial x_i \, \partial x_j}\right), \qquad \mathbf{H}^k = (H^k_{ij}) = \left(\frac{\partial^2 x_k}{\partial \xi_i \, \partial \xi_j}\right),$$

where $v = (v_0, v_1, v_2)$ is the unit fibre direction vector. These matrices are linked by the relations

$$\mathbf{W} = \mathbf{S}\mathbf{J},$$
$$T^k_{mp} = -\sum_l J_{kl} (\mathbf{J}^T \mathbf{H}^l \mathbf{J})_{mp}.$$

The Laplacian can be written as

$$\operatorname{div}(\mathbf{D} \operatorname{grad} u) = \sum_k p_k \cdot \frac{\partial u}{\partial \xi_k} + \sum_{k,l} q_{kl} \cdot \frac{\partial^2 u}{\partial \xi_k \, \partial \xi_l},$$

where

$$p_k = D_2 \operatorname{tr} \mathbf{T}^k + (D_1 - D_2) \cdot \Big((\mathbf{J}\mathbf{v})_k \cdot \operatorname{tr}(\mathbf{S}\mathbf{J}) + (\mathbf{J}\mathbf{S}\mathbf{J}\mathbf{v})_k + \mathbf{v}^{\mathrm{T}} \mathbf{T}^k \mathbf{v} \Big),$$

and q_{kl} are elements of matrix $\mathbf{Q}$:

$$\mathbf{Q} = \mathbf{J}\mathbf{D}\mathbf{J}^{\mathrm{T}}.$$

6.2. The no-flux boundary conditions in the special coordinates

The boundary condition

$$\mathbf{n}\mathbf{D} \operatorname{grad} u = 0, \tag{12}$$

where $\mathbf{n}$ is the normal vector to the LV surface, can be written in the form

$$\mathbf{n}^{\mathrm{T}} \mathbf{D} \mathbf{J}^{\gamma} \frac{\partial u}{\partial \gamma} + \mathbf{n}^{\mathrm{T}} \mathbf{D} \mathbf{J}^{\psi} \frac{\partial u}{\partial \psi} + \mathbf{n}^{\mathrm{T}} \mathbf{D} \mathbf{J}^{\varphi} \frac{\partial u}{\partial \varphi} = 0, \tag{13}$$

Preprints (www.preprints.org) | NOT PEER-REVIEWED | Posted: 8 August 2016 doi:10.20944/preprints201608.0080.v1

where $\mathbf{J}^{\gamma,\psi,\varphi}$ are the vector-columns of derivatives of the special coordinates with respect to Cartesian ones:

$$\mathbf{J}^{\gamma} = \begin{pmatrix} \gamma_x \\ \gamma_y \\ \gamma_z \end{pmatrix}$$

and so on. We use the method of fictitious nodes and make an additional layer of nodes outside the LV model. Values of the potential are found based on first-order derivatives with respect to the special coordinates. This method allows us to calculate the Laplacian in all non-fictitious nodes, be it points on the LV boundary or in its depth, on a consistent basis.

For the endo- and epicardium, equation (13) has to be solved for $\frac{\partial u}{\partial \gamma}$. Then, we find the potential at the fictitious node behind the endocardium (in the LV cavity) or the epicardium, respectively.

For the LV base, we transform equation (12) to form

$$\sum_k \left(\sum_j D^{2j} \frac{\partial \xi_k}{\partial x_j} \right) \frac{\partial u}{\partial \xi_k} = 0,$$

and express $\frac{\partial u}{\partial \psi}$:

$$\frac{\partial u}{\partial \psi} = -\frac{\left(D^{20}\gamma_x + D^{21}\gamma_y + D^{22}\gamma_z\right)\frac{\partial u}{\partial \gamma} + \left(D^{20}\varphi_x + D^{21}\varphi_y + D^{22}\varphi_z\right)\frac{\partial u}{\partial \varphi}}{D^{20}\psi_x + D^{21}\psi_y + D^{22}\psi_z}.$$

The required derivatives can be found numerically. The fictitious node is located above the LV base.

6.3. The method to rarefy the computation mesh

Let us consider a mesh node with indices i, j, k of special coordinates γ, ψ, ϕ. In the case of the symmetric LV model, we propose that its γ- and ψ-neighbours have indices $i \pm 1$, $j \pm 1$. Its ϕ-neighbours have indices $k \pm Q[j]$, where Q is an array of natural numbers, and the differences are found so that the Cartesian distances between nodes are within some given limits. In the case of the non-symmetric LV model, we have to introduce six arrays instead of one, Q^{dir}_{var}, where $var \in \{\gamma, \psi, \phi\}$, $dir \in \{+1, -1\}$. The meaning of Q^{dir}_{var} is that the index of γ-neighbour of the node in direction dir is $i + dir \cdot Q^{dir}_{\gamma}$. The index of ψ-neighbour in direction dir is $j + dir \cdot Q^{dir}_{\psi}$. The index of ϕ-neighbour in direction dir is $k + dir \cdot Q^{dir}_{\phi}$. The values of Q have to be found once, at the initialization stage. If for a node (i, j, k) at least one of $Q^{dir}_{var}[i][j][k]$ cannot be found, this node is marked 'out-of-mesh'. We compute the potential in this node not by a finite difference method but by interpolation, using the node's closest 'in-mesh' neighbours.

The flowchart in Fig. 15 depicts all the steps of construction and the use of the model in electrophysiological simulations.

7. An example of the spline-based model's practical usage in electrophysiological simulations

The model was used to study the dynamics of scroll waves of electrical excitation. Such waves are solutions of classical reaction-diffusion systems, and they correspond to dangerous arrhythmias, such as paroxysmal ventricular tachycardia and ventricular fibrillation. Our simulation was based on the Aliev–Panfilov model [8] of electrical excitation in the myocardium and the aforementioned

Preprints (www.preprints.org) | NOT PEER-REVIEWED | Posted: 8 August 2016 doi:10.20944/preprints201608.0080.v1

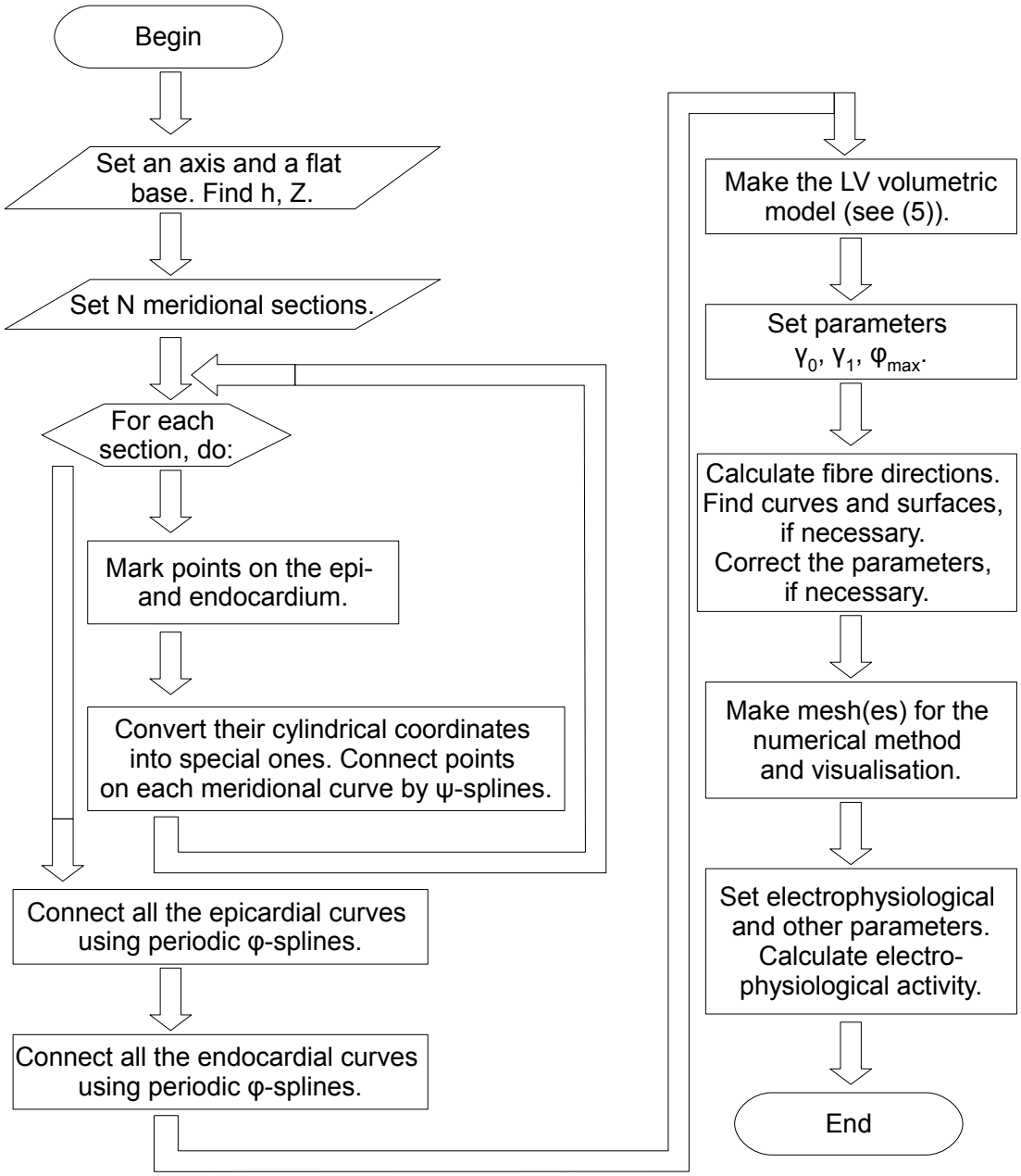

Figure 15. Flowchart displaying the steps for the construction and use of the spline-based LV model.

Preprints (www.preprints.org) | NOT PEER-REVIEWED | Posted: 8 August 2016 doi:10.20944/preprints201608.0080.v1

DT-MRI dataset and anatomical model (see Sections 2.4 and 4). The electrophysiological model is dimensionless and has the following form:

$$\begin{aligned} \frac{\partial u}{\partial t} &= \operatorname{div}(D \operatorname{grad} u) - ku(u-a)(u-1) - uv, \\ \frac{\partial v}{\partial t} &= \epsilon(u,v)(-v - ku(u-a-1)), \\ \epsilon(u,v) &= \epsilon_0 + \frac{\mu_1 v}{u+\mu_2}, \end{aligned} \tag{14}$$

where u is the transmembrane potential, v is the conductivity for the K current in the membrane, $D_{1,2}$ are diffusion coefficients along and across fibres, and k, a, ϵ_0, μ_1, μ_2 are cell model parameters. These parameters had the values $D_1 = 7.12$ mm^2/ms, $D_2 = D_1/9$, $k = 8$, $a = 0.1$, $\epsilon_0 = 0.01$, $\mu_1 = 0.12$, $\mu_2 = 0.3$. A boundary condition provided zero flux through the LV boundary. Initial conditions were $u = 1$, $v = 0$ (initial stimulation) at $\psi \le 0.4 \cdot \pi/2$, $0 \le \phi \le 2\pi/12$; $u = 0$, $v = k$ (initial temporary block of propagation) at $\psi \le 0.4 \cdot \pi/2$, $2\pi/12 \le \phi \le 2\pi/6$; and $u = 0$, $v = 0$ (resting state) elsewhere.

We used the spatial mesh size $dr = 0.5$ mm; the time step $dt = 0.01$ ms; and the dimension coefficients 5.4 ms, as the model time unit, and 6.2 mm, as the model length unit, based on the period and wavelength of a spiral wave simulated on a flat isotropic surface. The duration of the simulation was 10 sec.

The results we obtained are shown in Fig. 16, 17. From these results, we can see that the solitary filament drifted towards the base ($\psi = 0$), and then several filaments appeared. The number of filaments slowly increased from 1 to 9 and then decreased to 5-6. This observation means that a tachycardia paroxysm transformed into a fibrillation.

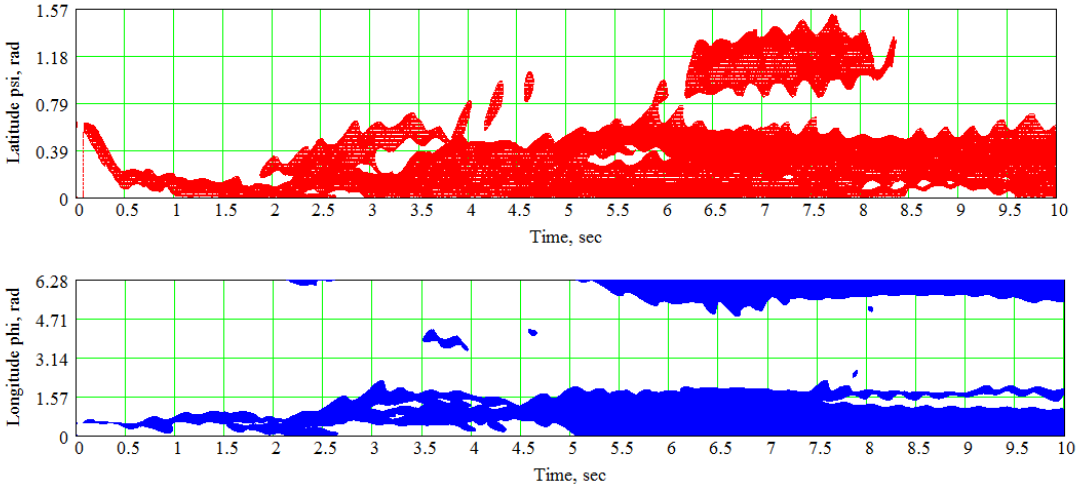

Figure 16. The special coordinates ψ and ϕ of the scroll wave filaments.

8. Discussion

This section analyses the algorithm, compares it with other models and techniques, examines its methods of verification, and concerns the usage and further development of the constructed model.

8.1. Advantages and disadvantages of the proposed model

The model adequately reproduces the fibre angles in the LV free wall and in the middle zone of the IVS of the human heart. Nevertheless, the data agreement in the apical zone of the IVS is only qualitative; in the IVS upper part of the human heart, the model yields results that differ from the experimental data.

Preprints (www.preprints.org) | NOT PEER-REVIEWED | Posted: 8 August 2016 doi:10.20944/preprints201608.0080.v1

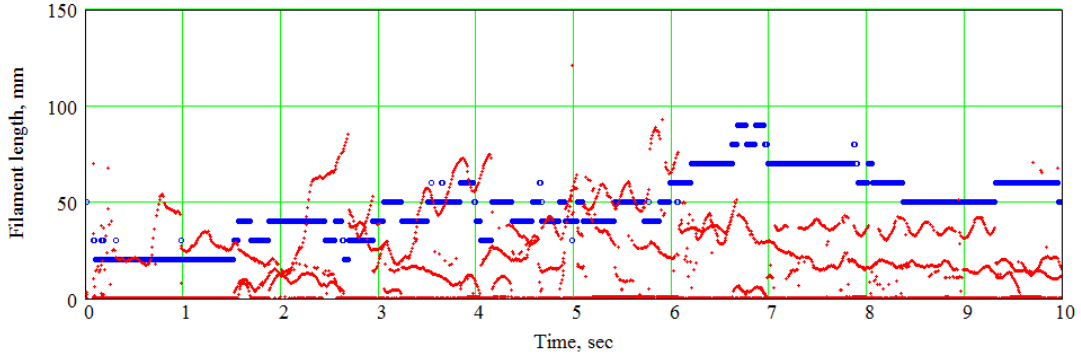

Figure 17. The number of filaments ($\times 10$; blue circles) and their lengths (red dots).

Our model has the following merits:

- It has relatively few parameters for shape, fibres and sheets.
- The LV apex is smooth thanks to the special choice of function z. This is a useful feature for integration methods sensitive to the smoothness of the boundary.
- It uses only simple 1-variable splines, and no 2- or 3-parametric splines are required.
- The fitting of shape and fibre directions are independent tasks in this model.
- It is flexible enough to fit not only normal but pathological LVs.
- It yields not only fibres but also sheets.

Limitations of the model include the following:

- Similar to our previous models, its base is flat, which is not the case in real mammal anatomy.
- The fibres are not geodesic lines in the model sheets. It is difficult to determine if this is a disadvantage of the fibres, the sheets or both.
- Model fibres end at the base. However, this demerit can be amended by combining this model with the toroids-based one described in [9].
- It is unclear whether the model is generalisable for both ventricles.

8.2. The present model compared with other qualitative models

The ventrucilar myocardium's structure and its qualitative description have been explored for several centuries. Reviews of experimental findings and theoretical conceptions can be found, for example, in [10,11] and other reviews in the Supplementary Volume [12]. The present model is conceptually close to Krehl's nested toroids to the extent that the LV myocardium, except the papillary muscles, is filled by nonoverlapping surfaces, and each surface is filled by nonoverlapping curves. The distinctive feature of the proposed model is the spiral shape of the surfaces. Whether the SSs are close enough to real heart sheets is a topic for future research.

In [4], Streeter proposed the geodesic principle of winding fibres on the sheets. This principle holds in the toroidal model but not in the present one. However, if we keep the fibres only, the surfaces may be adjusted to them. This interesting problem remains for future research: How should we draw a set of nonoverlapping surfaces on the given set of curves so that the curves are geodesic on the surfaces?

Some qualitative models of the myocardium describe its structure on the levels of cells, myofibres and myolaminae (see, for example, [13–15]); such models examine interconnetions and arrangement of cardiomyocytes and other types of cardiac cells. However, the main task of our model is to yield fibre and sheet normal directions in all points of the LV myocardium but not to represent the amazingly complex micro- and macrostructure of the cardiac muscle. A union of our model with a structural tissue-level model which includes Y-junctions of the cells, capillaries, fibrous tissue and other elements would be of great practical value.

Preprints (www.preprints.org) | NOT PEER-REVIEWED | Posted: 8 August 2016 doi:10.20944/preprints201608.0080.v1

A key feature of the proposed model is its numerical, quantitative nature, so it should be compared with other quantitative models and data.

8.3. Comparison with experimental data and quantitative models

Some experimental techniques that can be used to verify our model have been mentioned in our previous work [1]. They include DT-MRI (already used here) as well as micro-CT [16], histological investigation [17] and quantitative polarized light microscopy [18].

Experimental data on the fibre orientation obtained as described above may be used for the construction of anatomical computational models in different ways:

- as a discrete dataset in finite element models [19–21],
- or for the verification of rule-based models, i.e. the models formed on the basis of some constitutive rule [22–25].

A comparison with a recent rule-based method, the Laplace–Dirichlet algorithm [24], and with a wrapping-based myocardium model [26] was done in our pevious paper [1]. The idea of using splines to fit cardiac imaging data is not new. An example of such LV shape model, constructed with B-splines, together with a review of spline-based models can be found in [27]. A common weak point of many such models, however, is a lack of computing fibre direction field.

A quantitative comparison with a model from [24] can be made by measuring the mean difference angle between the experimental and model data. Bayer et al. in [24] report that their result is $23^\circ \pm 20^\circ$. Our result is $21^\circ \pm 18^\circ$, which is comparable with their achievement.

Our model fits the shape of the LV and has only three parameters (γ_0, γ_1, $\phi_{\max}$) to adapt fibre directions. Fibre directions can also be fitted through widely used fitting functions with many more parameters as it was done in [28]. In that work, fibre direction field in mice was approximated in spheroidal coordinates by a product of two algebraic and one trigonometric polynomials. A certain advantage of that approach is its flexibility. The reported root-mean-square error was about 2.3–10°. Yet, that method usually requires about 10 parameters for each algebraic and 10–40 for trigonometric polynomials, whereas our technique uses only 3 parameters. Also, the parameters in [28] have unclear geometrical or physical meaning, unlike ours. Moreover, the numbers of those parameters for different hearts vary, so the coefficients cannot be averaged to obtain *recommended* species-level parameter sets. We hope that our parameters can be averaged or fitted on the species level or at least for the norm and pathologies of particular species. This will allow researchers to construct fibre direction fields based on the shape of patients' hearts without DT-MRI data.

8.4. Further development and usage of the model

The model does not include the uppermost part of the ventricular myocardium, the basal ring, where myofibres form torus-like shapes [29, Fig. 14]. Moreover, some of the data available on the apical region show that myofibres there make toroidal layers, similar to basal ones [29, Fig. 6].

The spline apparatus enables researchers to use this model in cases of complex wall geometry, such as in patients with old myocardial infarctions, and other situations where the wall has locuses of thickening and thinning.

The analytical description of cardiac geometry has been used in developing a new numerical method for the study of the electrophysiological activity of the LV. The model can also be utilised to generate different anisotropical properties of the heart, to alter the LV shape (by changing the model parameters) and to study their influence on cardiac electrical and mechanical functions.

Acknowledgments: The author is grateful to Tatyana V. Chumarnaya for providing the sonography image used in this work; to Anton A. Koshelev for his help with DT-MRI data scaling. This work is supported by The Russian Science Foundation (Project 14-35-00005).

Conflicts of Interest: The authors declare no conflict of interest. The founding sponsors had no role in the design of the study; in the collection, analyses, or interpretation of data; in the writing of the manuscript, and in the decision to publish the results.

Abbreviations

The following abbreviations are used in this manuscript:

CT: computed tomography
DT-MRI: diffusion tensor magnetic resonance imaging
DTI: diffuse tensor imaging
IVS: interventricular septum
LV: left ventricle
RV: right ventricle
SS: spiral surface

Bibliography

1. Pravdin, S. Non-axisymmetric mathematical model of the cardiac left ventricle anatomy. *Russian Journal of Biomechanics* **2013**, *17*, 75–94.
2. Pettigrew, J. On the arrangement of the muscular fibers of the ventricular portion of the heart of the mammal. *Proc. Roy. Soc., London* **1860**, *10*, 433–440.
3. Pravdin, S.; Berdyshev, V.; Panfilov, A.; Katsnelson, L.; Solovyova, O.; Markhasin, V. Mathematical Model of the Anatomy and Fibre Orientation Field of the Left Ventricle of the Heart. *Biomedical Engineering Online* **2013**, *54*, 1–21.
4. Streeter, D., Handbook of physiology. Sec. 2. Vol. I. The Heart; Bethesda, Maryland: Am. Physiol. Soc, 1979; chapter Gross morphology and fiber geometry of the heart, pp. 61–112.
5. Pravdin, S.; Dierckx, H.; Katsnelson, L.; Solovyova, O.; Markhasin, V.; Panfilov, A. Electrical Wave Propagation in an Anisotropic Model of the Left Ventricle Based on Analytical Description of Cardiac Architecture. *PLOS One* **2014**, *9*, e93617. doi:10.1371/journal.pone.0093617.
6. Pravdin, S.; Dierckx, H.; Markhasin, V.; Panfilov, A. Drift of scroll wave filaments in an anisotropic model of the left ventricle of the human heart. *Biomed Research International Journal* **2015**, *2015*, 1–13.
7. Pravdin, S. A method of solving reaction-diffusion problem on a non-symmetrical model of the cardiac left ventricle. Proceedings of the 47th International Youth School-conference «Modern Problems in Mathematics and its Applications», Yekaterinburg, Russia. IMM Urb RAS, Yekaterinburg, 2016, pp. 284–296.
8. Aliev, R.; Panfilov, A. A simple two-variable model of cardiac excitation. *Chaos, Solitons and Fractals* **1996**, *7*, 293–301.
9. Koshelev, A.; Pravdin, S.; Ushenin, K.; Bazhutina, A.; Katsnelson, L.; Solovyova, O. A modified mathematical model of the anatomy of the cardiac left ventricle. *Biofizika* **2016**, *61*. accepted; in Russian.
10. Gilbert, S.H.; Benson, A.P.; Li, P.; Holden, A.V. Regional localisation of left ventricular sheet structure: integration with current models of cardiac fibre, sheet and band structure. *European Journal of Cardio-Thoracic Surgery* **2007**, *32*, 231–249.
11. Kocica, M.J.; Corno, A.F.; Carreras-Costa, F.; Ballester-Rodes, M.; Moghbel, M.C.; Cueva, C.N.; Lackovic, V.; Kanjuh, V.I.; Torrent-Guasp, F. The helical ventricular myocardial band: global, three-dimensional, functional architecture of the ventricular myocardium. *European Journal of Cardio-Thoracic Surgery* **2006**, *29*, S21–S40.
12. Rethinking the Cardiac Helix: A Structure/Function Journey, 2006. European Journal of Cardio-Thoracic Surgery, Vol. 29, S1.
13. Rushmer, R.; Crystal, D.; Wagner, C. The functional anatomy of ventricular contraction. *Circ Res* **1953**, *1*, 162–170.
14. Anderson, R.H.; Ho, S.Y.; Redmann, K.; Sanchez-Quintana, D.; Lunkenheimer, P.P. The anatomical arrangement of the myocardial cells making up the ventricular mass. *European Journal of Cardio-Thoracic Surgery* **2005**, *28*, 517–525, [http://ejcts.oxfordjournals.org/content/28/4/517.full.pdf+html].
15. LeGrice, I.; Smaill, B.; Chai, L.; Edgar, S.; Gavin, J.; Hunter, P. Laminar structure of the heart: ventricular myocyte arrangement and connective tissue architecture in the dog. *Am J Physiol* **1995**, *269*, H571–582.
16. Aslanidi, O.; Nikolaidou, T.; Zhao, J.; Smaill, B.; Gilbert, S.; Holden, A.; Lowe, T.; Withers, P.; Stephenson, R.; Jarvis, J.; Hancox, J.; Boyett, M.; Zhang, H. Application of Micro-Computed Tomography With Iodine

Staining to Cardiac Imaging, Segmentation, and Computational Model Development. *Medical Imaging, IEEE Transactions on* **2013**, *32*, 8–17.

17. Trew, M.; Caldwell, B.; Sands, G.; LeGrice, I.; Smaill, B. Three-dimensional cardiac tissue image registration for analysis of in vivo electrical mapping. *Ann Biomed Eng* **2011**, *39*, 235–248.
18. Jouk, P.; Usson, Y.; Michalowicz, G.; Grossi, L. Three-dimensional cartography of the pattern of the myofibres in the second trimester fetal human heart. *Anat Embryol (Berl).* **2000**, *202*, 103–118.
19. Vicky, Y.W. Modelling In Vivo Cardiac Mechanics using MRI and FEM. PhD thesis, Auckland Bioengineering Institute, The University of Auckland, New Zealand, 2012.
20. Gurev, V.; Lee, T.; Constantino, J.; Arevalo, H.; Trayanova, N. Models of cardiac electromechanics based on individual hearts imaging data: Image-based electromechanical models of the heart. *Biomech Model Mechanobiol* **2011**, *10*, 295–306.
21. Zhang, Y.; Liang, X.; Ma, J.; Jing, Y.; Gonzales, M.J.; Villongco, C.; Krishnamurthy, A.; Frank, L.R.; Nigam, V.; Stark, P.; Narayan, S.M.; McCulloch, A.D. An atlas-based geometry pipeline for cardiac Hermite model construction and diffusion tensor reorientation. *Medical Image Analysis* **2012**, *16*, 1130–1141.
22. Seemann, G. Modeling of Electrophysiology and Tension Development in the Human Heart. PhD thesis, Universitat Karlsruhe, 2005.
23. Bishop, M.J.; Plank, G.; Burton, R.A.B.; Schneider, J.E.; Gavaghan, D.J.; Grau, V.; Kohl, P. Development of an anatomically detailed MRI-derived rabbit ventricular model and assessment of its impact on simulations of electrophysiological function. *Am J Physiol Heart Circ Physiol.* **2010**, *298*, H699–H718.
24. Bayer, J.; Blake, R.; Plank, G.; Trayanova, N. A Novel Rule-Based Algorithm for Assigning Myocardial Fiber Orientation to Computational Heart Models. *Ann Biomed Eng.* **2012**.
25. Hren, R. A Realistic Model of the Human Ventricular Myocardium: Application to the Study of Ectopic Activation. PhD thesis, Halifax, Nova Scotia, Canada: Dalhousie University, 1996.
26. Sinha, S.; Stein, K.M.; Christini, D.J. Critical role of inhomogeneities in pacing termination of cardiac reentry. *Chaos: An Interdisciplinary Journal of Nonlinear Science* **2002**, *12*, 893–902.
27. Li, J.; Denney, T.S.J. Left ventricular motion reconstruction with a prolate spheroidal B-spline model. *Physics in Medicine and Biology* **2006**, *51*, 517–537.
28. Merchant, S.S.; Gomez, A.D.; Morgan, J.L.; Hsu, E.W. Parametric modeling of the mouse left ventricular myocardial fiber structure. *Annals of Biomedical Engineering* **2016**.
29. Torrent-Guasp, F. *The Cardiac Muscle*; Madrid: Fundacion Juan March, 1973.